Journal of
Instrumentation

PAPER • **OPEN ACCESS**

Quality control of plastic scintillators for the total-body J-PET scanner

To cite this article: Ł. Kapłon *et al* 2025 *JINST* **20** P09019

Published by IOP Publishing for Sissa Medialab

Received: *August 9, 2024*
Revised: *March 6, 2025*
Accepted: *August 13, 2025*
Published: *September 11, 2025*

Quality control of plastic scintillators for the total-body J-PET scanner

Ł. Kapłon,[a,b,c,*] **E. Beyene,**[a,b,c] **N. Chug,**[a,b,c] **C. Curceanu,**[d] **E. Czerwiński,**[a,b,c] **M. Das,**[a,b,c] **K. Eliyan,**[a,b,c] **K. Kacprzak,**[a,b,c] **T. Kaplanoglu,**[a,b,c] **G. Korcyl,**[a,b,c] **K. Kubat,**[a,b,c] **D. Kumar,**[a,b,c] **E. Lisowski,**[e] **F. Lisowski,**[e] **J. Mędrala-Sowa,**[a,b,c] **G. Moskal,**[b,c,f] **W. Mryka,**[a,b,c] **S. Niedźwiecki,**[a,b,c] **P. Pandey,**[a,b,c] **S. Parzych,**[a,b,c] **E. Pérez del Rio,**[a,b,c] **S. Sharma,**[a,b,c] **M. Skurzok,**[a,b,c] **P. Tanty,**[a,b,c] **K. Tayefi,**[a,b,c] **A. Venadan,**[a,b,c] **E. Stępień**[a,b,c] **and P. Moskal**[a,b,c]

[a] *Faculty of Physics, Astronomy and Applied Computer Science, Jagiellonian University,*
Łojasiewicza 11 St., 30-348 Kraków, Poland
[b] *Total-Body Jagiellonian-PET Laboratory, Jagiellonian University,*
Łojasiewicza 11 St., 30-348 Kraków, Poland
[c] *Center for Theranostics, Jagiellonian University,*
Kopernika 40 St., 31-034 Kraków, Poland
[d] *INFN, Laboratori Nazionali di Frascati,*
Via E. Fermi 40, 00044 Frascati, Italy
[e] *Faculty of Mechanical Engineering, Cracow University of Technology,*
al. Jana Pawła II 37, 31-864 Kraków, Poland
[f] *Faculty of Chemistry of the Jagiellonian University,*
Gronostajowa 2, 30-387 Kraków, Poland

E-mail: `lukasz.kaplon@uj.edu.pl`

Abstract: The construction of the total-body Jagiellonian positron emission tomography scanner requires component verification before detector assembly. The purpose of this research is to verify the quality of BC-408 plastic scintillators with dimensions $6\,mm \times 30\,mm \times 330\,\mathrm{mm}$. The scintillators were inspected for optical and mechanical defects and all dimensions were measured. Scratches, mechanically damaged corners and edges, as well as encapsulated dust and fibers within the scintillators, were identified under ceiling lamp illumination. Line defects on the as-cast surfaces were easily visible in a plane polariscope setup consisting of crossed horizontal and vertical polarizer foils. The transmittance at the wavelength of maximum emission through 6 mm thick scintillator samples and the technical attenuation length along 330 mm long scintillator samples were measured on a linear CCD array spectrometer for randomly selected scintillators from each delivered batch. Selected properties of the emission spectra, such as their FWHM and the values of the emission maxima as a function of the distance between the excitation point and the spectrometer fiber, were measured. Additionally,

---

[*] Corresponding author.

https://doi.org/10.1088/1748-0221/20/09/P09019

the scintillators optical homogeneity was measured on a light transfer setup consisting of an LED and photodiode matrix. The majority of the obtained plastic scintillators meets the transparency criteria and falls within the dimensional tolerances.

KEYWORDS: Scintillators and scintillating fibres and light guides; Scintillators, scintillation and light emission processes (solid, gas and liquid scintillators); Gamma detectors (scintillators, CZT, HPGe, HgI etc)

Contents

1 Introduction

Positron emission tomography (PET) imaging is the best method for quantitatively assessing disease stages at the cellular and molecular levels [1]. The development of modern PET scanners with a long axial field of view enables the simultaneous imaging of the patient's entire body [2]. Currently, three total-body PET scanners are based on crystal scintillators: Explorer and PennPET Explorer utilize LYSO, lutetium-yttrium oxyorthosilicate [3, 4], and Biograph Vision Quadra utilizes LSO, lutetium oxyorthosilicate [5]. Coincidence resolving time and depth of interaction in PET detectors can be improved by using the crosshair light-sharing method between crystals in a scintillator array [6] and by avoiding optical crosstalk in the protective cover of silicon photomultiplier arrays [7]. A new generation of cost-effective PET scanners can be based on Compton imaging [8] and double-photon emission imaging [9], which can provide multi-molecule or multi-nuclide imaging [10].

The cost-effective total-body Jagiellonian positron emission tomography (TB-J-PET) is based on long plastic scintillators [11] and uses Compton scattering as the primary mode of photon interaction [12, 13]. The different geometrical configurations of the TB-J-PET scanner [14] and its modular arrangement [15] can reduce the cost of the tomograph [13]. PET scanners built from plastic scintillators enable positronium imaging [16–18], multi-isotope imaging [19], testing of charge, parity, and time-reversal transformations [20], measurements of polarization of photons [21], quantum entanglement imaging [22], and proton beam therapy monitoring [23–25]. The design of TB-J-PET requires the usage of transparent plastic scintillators with low light attenuation [26] to build long modules with silicon photomultipliers attached at both ends of the scintillators. For the modular TB-J-PET construction, we choose BC-408, one of the most transparent plastic scintillator from our previous measurements [27].

In research projects building radiation detectors from thousands of scintillator elements, quality control (QC) of the components is carried out to ensure a uniform operation of the entire detector. Quality control of plastic scintillators and plastic scintillating fibers usually involves the following measurements: dimensions and dimensional uniformity, absolute or relative light yield, technical attenuation length and spectral response (table 1). To excite the scintillators, the following sources were used: ^{137}Cs, ^{57}Co, ^{60}Co gamma isotopes, ^{90}Sr beta isotope, ultraviolet and blue light-emitting diodes (LED), and a laser. Technical attenuation length or bulk attenuation length measurements were used to confirm the high light transmission of scintillators [28–30]. In projects using hundreds of thousands of scintillating fibers, between 0.5 and 1% of the fibers were randomly selected from each batch and tested to verify the properties of each delivered batch [28].

Table 1. Measurements performed during quality assurance before manufacturing of scintillation radiation detectors found in the literature.

Scintillator type	Scintillators quantity	Excitation source	Measured properties	Ref.
Plastic scintillators and plastic scintillating fibers				
SCSN-38	12 420	^{137}Cs	relative light yield	[31]
SCSN-81 BC-408	20 916	^{60}Co	absolute light yield	[32]
SCSF-3HF	22 365	^{57}Co, 405 nm LED	light yield, scintillating fiber matrix integrity	[33]
Extruded plastic scintillator	33 500	^{90}Sr, 440 nm laser	relative light yield, bulk attenuation length, dimensions	[30]
SCSF-78MJ	7.5×10^5	^{90}Sr, 373 nm LED	dimensional uniformity, spectral response, technical attenuation length	[28]
SCSF-78MJ	3.2×10^6	^{90}Sr	light yield, scintillating fiber matrix integrity	[34]
SCSF-78MJ	5.0×10^6	^{90}Sr, X-ray tube, 390 nm LED	light yield, diameter and cladding quality, radiation hardness, technical attenuation length	[29]
Inorganic crystal scintillators				
$PbWO_4$	1 000	^{22}Na, halogen lamp	dimensions, longitudinal and transversal transmission, decay time, relative light yield and its uniformity	[35]
CsI:Tl	6 340	^{137}Cs	relative light yield and its uniformity, radiation hardness	[36]
$PbWO_4$	30 600	^{60}Co, Xe lamp	dimensions, longitudinal and transversal transmission, absolute light yield and light collection uniformity	[37]
$PbWO_4$	80 000	^{22}Na	absolute light yield	[38]

Inorganic crystal scintillators were verified with the use of similar quality control methods. In order to check 80 000 pieces of $PbWO_4$, lead tungstate crystal scintillators, two automatic machines have been designed in the Compact Muon Solenoid collaboration for quality control before the electromagnetic calorimeter assembly [35, 37]. For each crystal, the machines were able to measure the dimensions in a few spots; a spectrophotometer assessed the longitudinal and transversal transmission; a photomultiplier tube (PMT) setup allowed for the measurement of decay time, relative light yield, and light yield uniformity across the crystal length. About 5 to 20% of the $PbWO_4$ crystals in each delivered batch were rejected [39] because of two main reasons: dimensions outside the tolerances, and transmission limits. One of the requirements of scintillators for an electromagnetic calorimeter is radiation hardness. A sample from each batch of CsI:Tl, thallium doped cesium iodide crystals was tested for radiation damage during quality control of 6 340 pieces of the crystal in the Beijing Spectrometer collaboration [36]. The relative light yield of CsI:Tl crystals and its uniformity were also verified.

The birefringence of optical materials can be used for quality evaluation of scintillators. Photoelasticity is a nondestructive method of residual stress inspection in optical materials [40]. The method is based on the analysis of the fringe pattern parameters observed in a plane or circular polariscope, for example, in birefringent crystal under compression load [41]. The birefringent properties of samples with internal stress residue cause the distortion of the interference fringes. Modern digital photoelasticity methods are applied in various engineering and science fields, such as biomedicine, rapid prototyping, mechanical components, composites, fracture and contact mechanics, semiconductors and electronic circuits manufacturing, monitoring process parameters of injection molded plastic components [42]. Photo-elastic analysis was used to map residual stress distributions in inorganic scintillation crystals (e.g., BGO, bismuth germanium oxide [43], YAG:Ce, cerium-doped yttrium aluminum garnet [44], $CaWO_4$, calcium tungstate [45], and $PbWO_4$, lead tungstate [46–48]). Photo-elastic measurements were not used for quality control of organic or plastic scintillators.

The purpose of this research is to perform quality control measurements of the plastic scintillators intended for the construction of two rings of the TB-J-PET scanner and verify their optical uniformity and transparency of the scintillators. Quality assurance of plastic scintillators in this work was done in few steps. Firstly, the scintillators were inspected by eye under white light illumination for the presence of defects on their surface or in their volume (section 3.1). The second step was the measurement of their dimensions with the use of calipers to reject scintillators outside of the dimensional tolerance limits (section 3.2). In the third step, the optical uniformity of the scintillators was measured utilizing LEDs to excite the scintillator and photodiode light detectors (section 3.3). Two additional measurements were performed on randomly selected scintillators from each delivered batch to verify their transverse and longitudinal transparencies: the transmittance at the wavelength of maximum emission (section 3.4) and the technical attenuation length (section 3.5); both measurements utilized a linear CCD array spectrometer.

2 Materials and methods

To assemble two rings of the total-body J-PET scanner 1570 pieces of BC-408 plastic scintillator were purchased from Luxium Solutions (U.S.A.), formerly Saint-Gobain Crystals. The chosen BC-408 scintillator type possesses some of the best scintillating and optical properties for the construction of long J-PET modules [27]. The scintillators were manufactured in 19 batches within 6 months of 2023. The quantity for two rings consists of scintillators for 24 modules in each ring, and in each module there are 2 layers of 16 scintillators separated by a layer of BC-482A wavelength shifter bars [13]. The scintillators have rectangular shape, 6 mm × 30 mm × 330 mm, polished surfaces “faces as-cast and edges diamond-milled”. The 6 mm × 30 mm cross section of the scintillator was chosen to attach four silicon photomultipliers at both ends of the scintillator, with an active light detection area of 6 mm × 6 mm per one photomultiplier [49].

Plastic scintillator manufacturers do not perform detailed quality control of each scintillator piece. In the factory, plastic scintillators pass through visual inspection of cast sheet after the polymerization process. The cast sheets are inspected for flatness, presence of release marks, mold or handling scratches or scuffs, grease or fingerprints on the surfaces, chips, dirt and particle contaminations in the scintillators bulk, and for color and haze.

Quality control of the plastic scintillators in the J-PET laboratories consists of five techniques: (1) visual inspection for optical and mechanical defects to qualify them for warranty replacement; (2) dimension measurements of each scintillator with the use of calipers and their comparison with the expected dimensions to qualify them for warranty replacement if any dimension of the scintillator exceeds the tolerance limit; (3) optical light transfer test of selected scintillators on a test setup consisting of exciting LED and matrix of photodiodes to confirm the optical homogeneity of the scintillators; (4) transmission spectra measurements of randomly chosen scintillators from each batch to confirm their high optical transmittance for the emitted light; (5) technical attenuation length measurements of randomly chosen scintillators from each batch to check the attenuation of the emitted light.

The visual inspection was performed by looking by eye at the scintillators under: (1) white background light from a ceiling lamp, (2) UV lamp with 405 nm maximum emission, (3) a setup with cross-polarized light. Defects like scratches, mechanically damaged corners and edges were found under light from a ceiling lamp. Encapsulated dust and fibers in the volume of the scintillators were found under UV light as glowing points on a black background or as shadows under the ceiling lamp on a white background. Release marks defects on the as-cast surfaces were easily visible in setup with cross-polarized light (figure 1). The inspected plastic scintillator is placed in a polariscope setup consisting of the following elements arranged linearly: white light source, first polarizer, scintillator sample, second polarizer called analyzer, focal plane or camera. The setup for finding release marks consisted of a 500 mm diameter white LED lamp with a diffuser and two pieces of linear polarizer foil with dimensions 500 mm × 500 mm. The surfaces of the foils were set up parallel to each other and the polarization patterns were crossed at right angles to each other. The first foil (horizontal polarizer) was attached to the LED lamp, the second foil (vertical polarizer) was attached to the frame placed on the table. Plastic scintillators were placed between the foils. Release mark defects were visible as sharp lines with black and white sides on a gray background. Examples of release mark defects are shown in figure 5a.

Dimension measurements were performed with the use of digital calipers: Limit CDN 200 mm for width and thickness (catalog number 28047-0204, accuracy ±0.03 mm) and Limit CDA 500 mm for length (catalog number 2289-0107, accuracy ±0.05 mm). Width and thickness were measured at two sides approximately 10 mm from both ends of the scintillator. The length of each scintillator piece was measured once. Dimension tolerances for the BC-408 scintillators are ±0.25 mm for width and length (from diamond-milling process) and ±0.58 mm for thickness (from casting process). The dimension tolerances are received from the manufacturer, and are adequate for the purpose of building the TB-J-PET.

An optical light transfer test is enforced to verify the optical homogeneity of the scintillators along their length and to quantitatively measure the symmetry of the light passing through each scintillator. An LED with wavelength of maximum emission positioned at 405 nm was used to excite the BC-408

2025 JINST 20 P09019

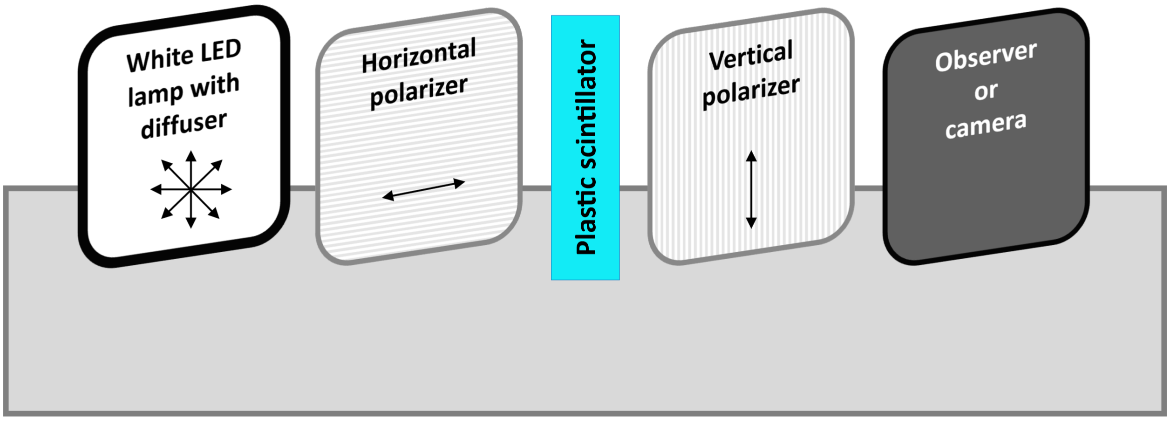

Figure 1. Scheme of the experimental setup with a plane polariscope designed to identify release mark defects using cross-polarized light.

plastic scintillator with wavelength of maximum emission at 425 nm [26]. The light emitted by the LED excites the scintillators through 6 mm of their thickness. Part of the light emitted inside of the scintillator is reflected to both ends because of total internal reflection. The light emitted by the scintillator that reaches the ends of the scintillator bar is detected by photodiodes mounted at both ends of the scintillator (figure 2). Voltage signals from the photodiodes are measured by two multimeters. The scintillators were excited by the LED at three positions along their length: 30 mm, 165 mm and 300 mm. At each position, the average signal voltage and its standard deviation, measured at both sides of the scintillator, were saved. The background noise voltages for both photodiode sides were also saved in the setup with the scintillator inserted and covered with a light-tight cover. The fractional change of the voltage measured on two scintillator sides for 30 mm and 300 mm positions, indicated with D, can be used as a measure of the scintillator optical homogeneity:

$$D = \frac{V_A - V_B}{0.5 \times (V_A - B_A + V_B - B_B)} \times 100\% \tag{2.1}$$

where V_A, V_B, B_A, and B_B denote the voltage signal from A side, B side and the background voltage from A and B sides, respectively. A big difference (more than 50% value of the difference D) of amplitudes measured at both ends indicates the presence of defects in the scintillator bulk [50].

The setup for the light-transfer test consists of two photodiode matrices (Osram BPW 34) reading blue light signal from the A and B ends of the scintillator sample, two multimeters (Rigol DM3068) for voltage signal readout from the A and B photodiode matrices, a black aluminum stabilizing rail for the scintillator and a light-tight cover with black rubber under the stabilizing rail for removing the influence of the visible light background. An LED (OptoSupply OSV5YL3131A, 3 mm diameter, 5 mW of radiant flux at the typical supply voltage of 3.1 V) was installed in the aluminum collimator to prevent light scattering and align the LED light to the middle of the scintillator width and perpendicular to the largest of the as-cast surfaces of the scintillator. Each photodiode matrix consisted of four individual photodiodes with a radiant sensitive area of 2.65 mm × 2.65 mm connected together into a linear array to sum of the voltage signals. The LED and photodiode matrices were powered by a Keysight E36312A power supply. A matte black microporous rubber was installed at the bottom of the stabilizing rail to prevent the LED light that passed through the scintillator to be reflected back into the scintillator.

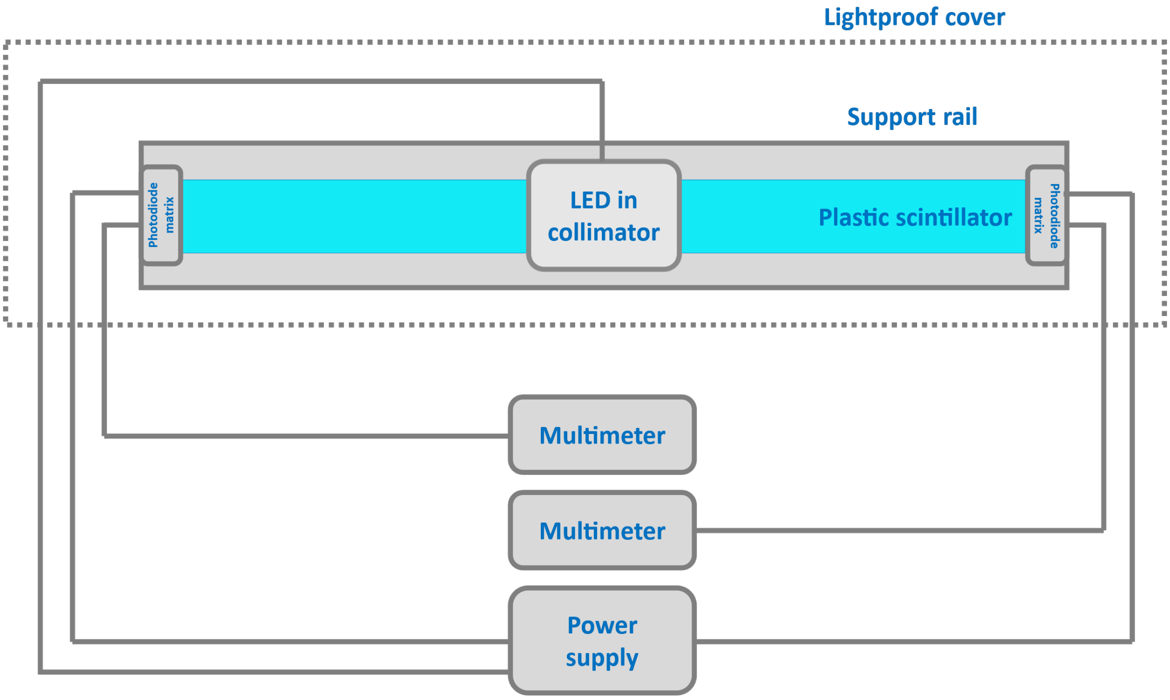

Figure 2. Scheme of the experimental setup for the light-transfer test.

The setup for the light transfer was tested with the use of three different LEDs with emission maxima centered at 385, 395 and 405 nm (OptoSupply, OSV3SL3131A, OSV4DL3131A and OSV5YL3131A). The LEDs have the same 3 mm diameter, 30° of 50% power angle and 10, 14 and 5 mW of radiant flux power for the 385, 395, and 405 nm LED, respectively. When a scintillator was inserted into the setup, the LEDs in the collimator would excite it in the middle of its length at position 165 mm. The LEDs were supplied with a voltage ranging between the minimum and maximum values defined in their data sheets, in 0.05 V increments. The average voltage signals from one photodiode matrix and their standard deviations, read out by the multimeters, were saved.

The emission and transmission spectra through 6 mm thick scintillator (relative to the air) were measured with the use of a fiber optic spectrometer (Ocean Optics, USB4000), a quartz-core optical fiber (Ocean Optics, P400-2-UV–VIS), a tungsten halogen lamp (Ocean Optics, LS-1), and a personal computer with the spectrometer software (figure 3). An ultraviolet (UV) lamp with maximum emission centered at 365 nm was used to excite the BC-408 plastic scintillator. To determine the maximum emission value, a Gaussian function was fitted to the emission spectrum in a small range, about 10 nm wide, around the peak emission value. For comparison, the FWHM of a typical emission spectrum of the BC-408 plastic scintillator is about 40–50 nm. An example of such a fit is shown in figure 12, right.

To measure transmittance, scintillators were inserted into a 6.4 mm thick slit between the fiber connector and the LS-1 lamp. Transmission spectra for each scintillator were measured for three points: in the middle of the scintillator, and about 20 mm from both ends of the scintillator. The obtained emission maximum at 425.8 nm was used to find the transmittance at the wavelength of the maximum emission point. To avoid small fluctuations of the transmittance measurement, ten equally spaced data points in the range 425–427 nm were averaged for each transmittance measurement point. For each scintillator, three measurements of the transmittance at the wavelength of maximum

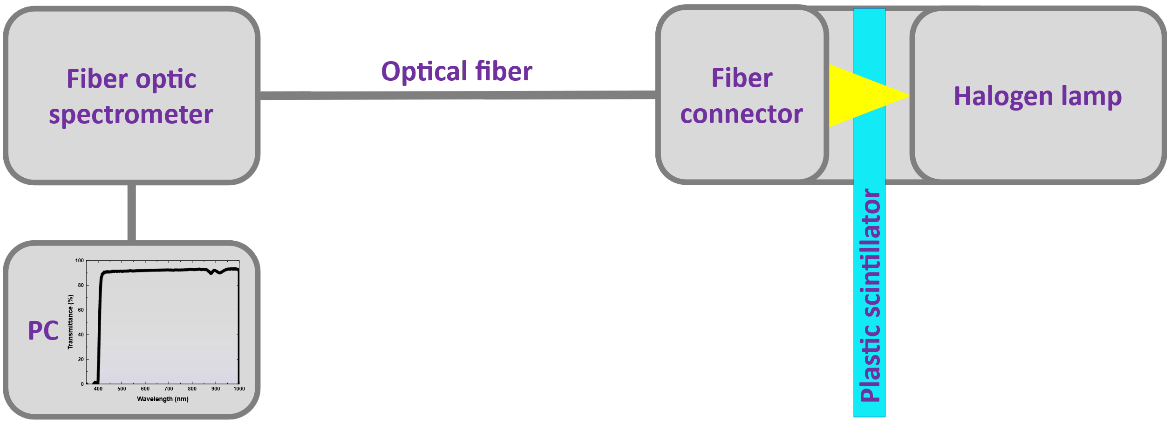

Figure 3. Scheme of the experimental setup for the transmittance measurement.

emission were performed; their average and standard deviation were then calculated. One scintillator from each of the nineteen batches obtained from the manufacturer was fully characterized. Batches usually contain from 75 to 90 pieces of the scintillator.

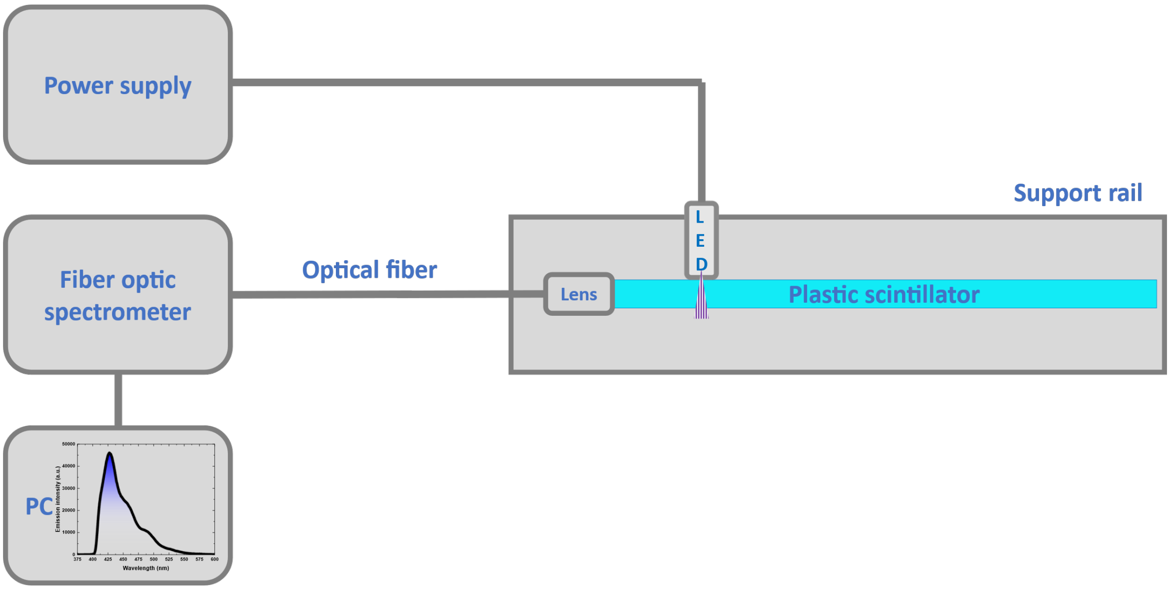

Figure 4. Scheme of the experimental setup for the measurement of the technical attenuation length.

The technical attenuation length (TAL) is the length of scintillator after which the signal strength of the emitted light drops by a factor $1/e$ from its initial value. The TAL includes the effect of the light absorption in the scintillator bulk and total internal reflections from the scintillator surfaces. The TAL was measured in a setup consisting of an exciting LED with its emission maximum centered at 405 nm (OptoSupply, OSV5YL3131A), a power supply for the LED (Keysight, E36312A), a collimating lens with 5 mm diameter (Ocean Optics, 74-UV) mounted to an optical fiber (Ocean Optics, QP450-1-XSR), spectrometer (Ocean Optics, SR-2UVV400-25), a computer with the OceanView spectroscopy software (figure 4). The LED, inserted in a collimator, excites the scintillator from the side, in 2 cm steps, perpendicular to its as-cast surface. A part of the emitted light reaches the

6 mm × 30 mm edge of the scintillator, where it is collected by the lens attached to the center of the edge and transmitted by the optical fiber to the spectrometer. Emission spectra were corrected in the OceanView software for the dark noise from the spectrometer. The highest value of the emission intensity was used to plot the emission intensity at the maximum of the emission spectrum versus the LED-fiber distance. The scintillators were too short to determine the long component of the TAL. To obtain the short component of the TAL, a single exponential function was fit to the data points:

$$I(x) = A \times e^{-\frac{x}{\lambda_S}} + y_0, \tag{2.2}$$

where λ_S is the short attenuation-length component, A is the amplitude, and y_0 is the background from the spectrometer.

3 Results and discussion

3.1 Defects

Many defects, such as mechanically damaged corners and edges, scratches and release marks on the surface, dust and fibers encapsulated in the volume of scintillator, were found in this work. Based on our previous orders from several manufacturers, we have found five common types of plastic scintillator defects:

1) Release marks — line defects imprinted on as-cast surfaces, these defects manifest as wavy lines barely seen under ambient light but easy visible with the use of a plane polariscope (figure 5(a)). The origin of the line defects can be the uneven detachment of the scintillator from the mold plates during the polymerization process or flaws imprinted on the scintillator from the mold plates;

2) Encapsulated particles — dust, dirt, particles and fibers encapsulated and polymerized in the scintillators. These defects are seen as spots with various shapes, colors and sizes up to a few millimeters present in the volume of scintillators. They can be easily detected by eye screening against the background of a uniform white lamp (figure 5(b)). The cause may be a lack of caution during the assembling and filling of the molds in an unclean environment;

3) Fluorescent defects — very bright areas in the volume of the scintillators seen under a UV lamp, with sizes up to few centimeters (figure 5(c)). These defects may result from an uneven mixture of several additions of prepolymer (a partially polymerized, highly viscous liquid monomer with fluorescent substances) to the same mold or from a failure during the polymerization process;

4) Microcracks (up to a few millimeters) – while the as-cast surface of the scintillator looks matte in ambient light, under a UV lamp the light escapes from the surface and glows in all directions (figure 5(d)). The polyvinyltoluene surface is prone to cracking from applied mechanical stress, exposure to organic vapors and high intensity light (especially UV light). These defects may originate from the polymerization process or from the mechanical processing, when high pressure is applied to the surface or the scintillator is exposed to vapors of organic solvents during the milling process;

5) Mechanical damage — examples of this type of defects are mechanically damaged corners and edges, partially not polished edges, very deep and long scratches, crooked cut edges revealing themselves as two nearby surfaces at one edge are not perpendicular. These defects are created as a result of mechanical processing or during transport of the scintillator.

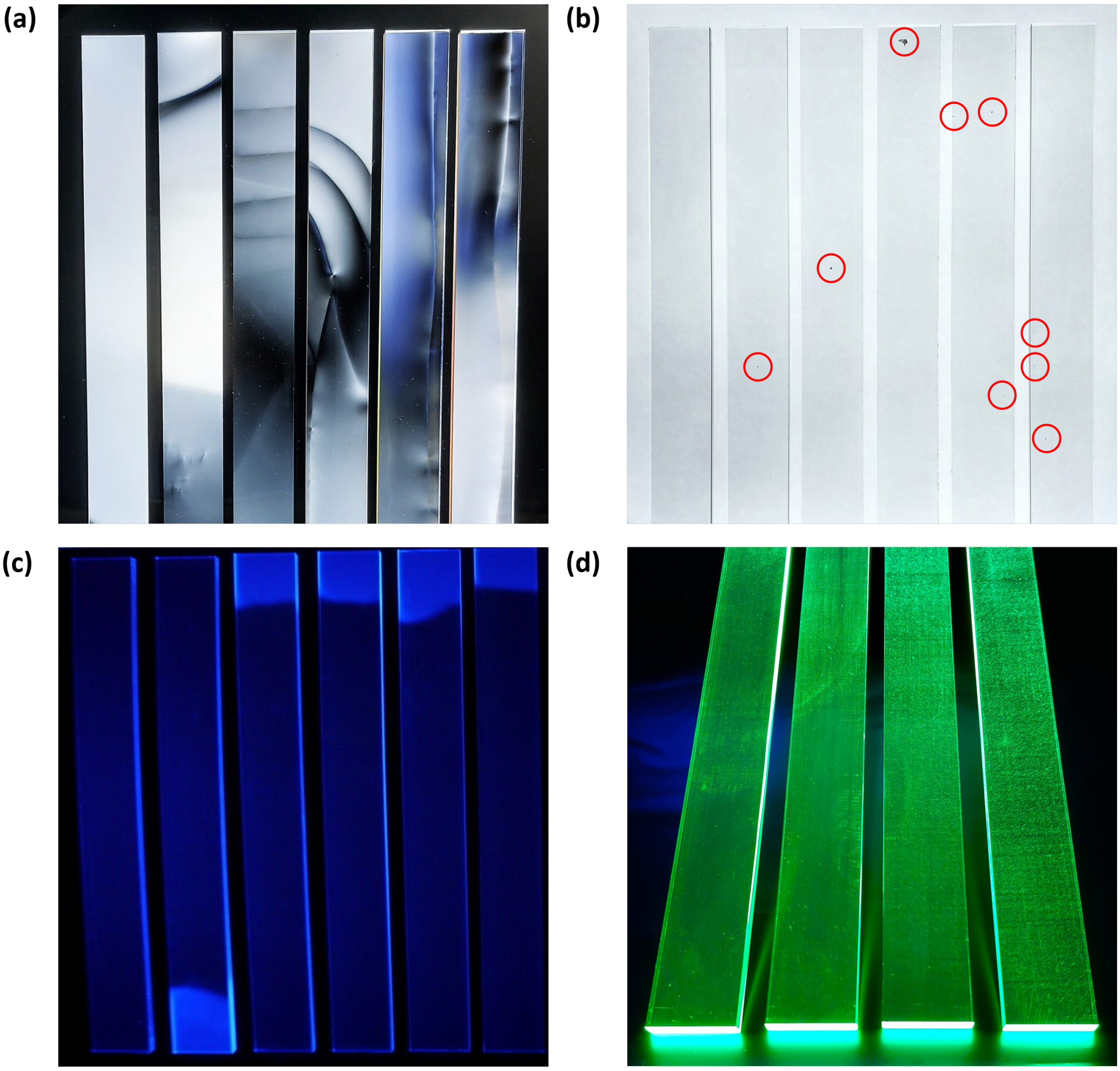

Figure 5. Defects in plastic scintillators: (a) release marks imprinted on as-cast surface of BC-408 scintillator viewed in plane polariscope; (b) encapsulated particles in the volume of BC-408 scintillators viewed against the background of a white lamp where the red circles denote the location of the defects; (c) fluorescent defects in the volume of BC-420 scintillators viewed under a UV lamp; (d) large amounts of microcracks on as-cast surface of EJ-260 scintillators viewed under a UV lamp (the two scintillators on the left side are without defects for a comparison). The leftmost scintillator in (a), (b), (c) is without defects and included for a comparison.

Defects occurred as release marks in 19.6% of the scintillator pieces, encapsulated particles in the volume of the scintillator (12.9%), exceeded dimensional tolerances (11.3%), and mechanical damage (3.5%) (figure 6). The warranty on release marks and encapsulated particles was rejected by the manufacturer. Release marks may exist on the scintillator surface, provided that the physical integrity

2025 JINST 20 P09019

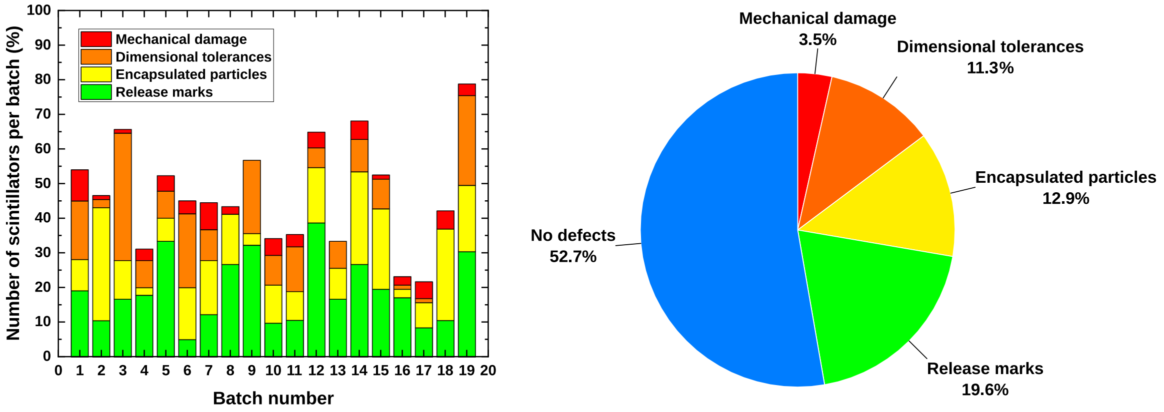

Figure 6. Distribution of the different defect types between 19 batches of plastic scintillator (left), and percentage of each defect type in the whole scintillator delivery (right).

of the scintillator is not compromised. The maximum allowable encapsulated particle size is 3.2 mm. Both defects do not affect the performance of the plastic scintillator unless there is a concentration of multiple defects in one scintillator or one defect type forms a concentrated pattern.

In total, 15% of delivered plastic scintillators were qualified for a replacement under the warranty, which covers dimensional tolerances and mechanical defects. A rejection ratio at the 15% level is similar to the one in other experiments involving the assembly of many pieces of scintillators. For example, a rejection ratio at the level of 16–20% was found for PWO crystals in the CMS electromagnetic calorimeter [35]. Smaller rejection ratios, at the level of 0.3% and 1.7–2.5%, occurred for detectors assembled from plastic scintillating fibers [29, 31].

3.2 Dimensions

Dimension distributions are plotted in figure 7. The means of the Gaussian distributions of the scintillator dimensions are at close distances of 0.02–0.13 mm from the ordered dimensions, 6 mm × 30 mm × 330 mm. Most scintillators were within the dimensional tolerance limits. In total, 88.66% of all scintillators fit within the combined dimension tolerance for thickness, width and length. A small portion of plastic scintillators failed the dimensional inspection in more than one dimension. The fractions of scintillators exceeding the dimensional tolerances are 2.36% for length, 2.68% for width and 6.82% for thickness.

The majority of the scintillators that fail the tolerance limit are cast scintillators, because the casting process has a wider tolerance range (±0.58 mm) than the diamond-milling process (±0.25 mm) on the width and length of the scintillators. The scintillator thickness has a wider distribution (0.25 mm) compared to the distributions of width and length (0.10 mm and 0.09 mm, respectively) because the casting process during the bulk polymerization may result in a thermal expansion or shrinkage of the mold that contributes to the spread of the thickness distribution [51].

The thickness and width differences at both ends of the same scintillator are presented in figure 8. For individual scintillator pieces, the dimensions difference between both ends fit into a maximum range that is twice as large as the tolerance range. The diamond milling process has the largest width differences, up to 0.2 mm. The casting process results in much larger differences on the thickness, up to 1.1 mm. This result will influence the assembling of the J-PET modules where scintillators

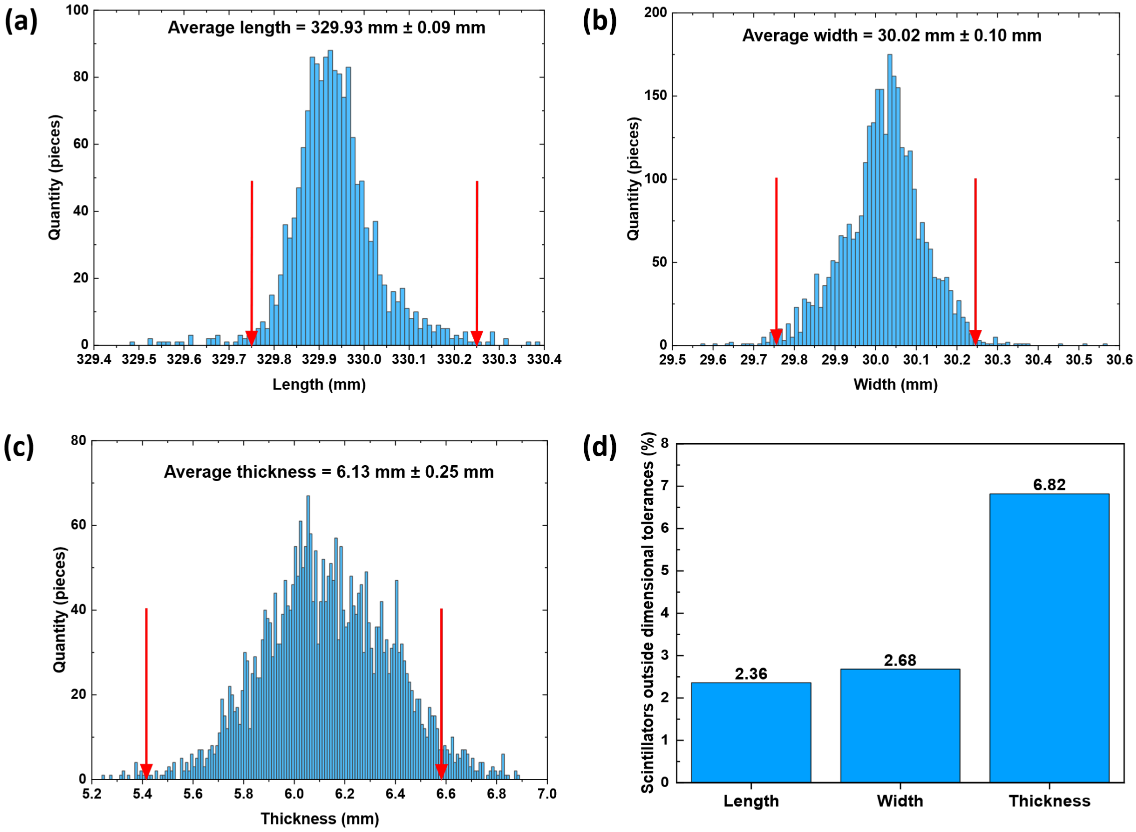

Figure 7. Dimension distributions of the BC-408 plastic scintillators for length (a), width (b), and thickness (c). The red arrows indicate the maximum dimensional tolerance ranges, ±0.25 mm for width and length, and ±0.58 mm for thickness. The binning of the histogram was set to 0.01 mm, which corresponds to the least significant digit in a caliper reading. The average dimension and its uncertainty correspond to the mean and standard deviation of the corresponding distribution. The percentage of scintillators exceeding the dimensional tolerances for length, width, and thickness (d).

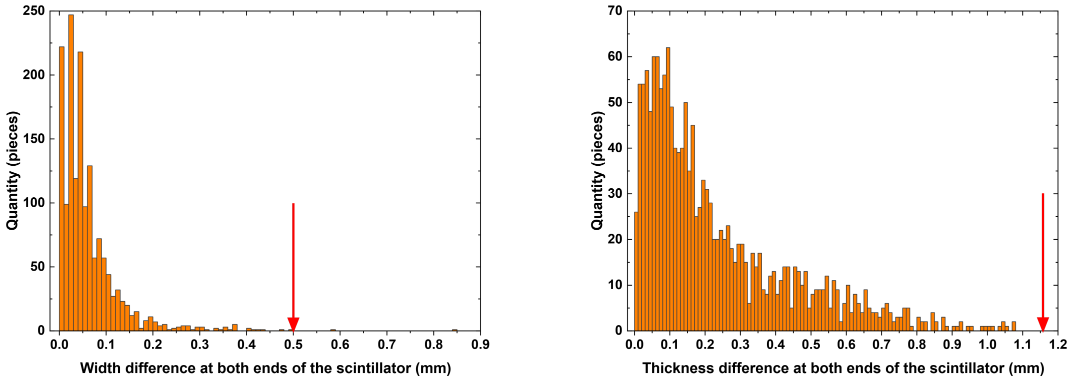

Figure 8. Dimensions differences at both ends of the scintillators for width (left) and thickness (right). The red arrows indicate the sum of two dimension tolerances ranges for one scintillator piece: 0.5 mm for width and 1.16 mm for thickness. The binning of the histogram was set to 0.01 mm, which corresponds to the least significant digit in a caliper reading.

with high dimensions differences at both ends should be rejected or fit into the module alternately (thick to thin side) to compensate for the dimension differences.

3.3 Optical homogeneity

Results from the testing setup for the light transfer with three different LEDs are presented in figure 9. On the left panel of figure 9, emission spectra of the LEDs superimposed on the absorption spectrum of the fluorescent dye POPOP (1,4-bis(5-phenyl-2-oxazolyl)benzene), which is used as wavelength shifter in plastic scintillators [52], are presented. The emission spectra of the LEDs were measured in this work. The absorption spectrum of the POPOP dye in a cyclohexane solution was taken from the PhotochemCAD database described in reference [53]. The emission maxima of the LEDs are located at 381.94 nm, 396.85 nm, and 402.74 nm. Even a slight overlap of the fluorescent dye's absorption spectrum with the LED emission spectrum causes scintillator excitation. The wavelength shifter component in the BC-408 scintillator is proprietary. The POPOP dye was chosen to explain the scintillators excitation because the dye has one of the best scintillating properties and its 422 nm emission maximum in polystyrene scintillator is very close to the 425 nm emission maximum of the BC-408 polyvinyltoluene scintillator [54].

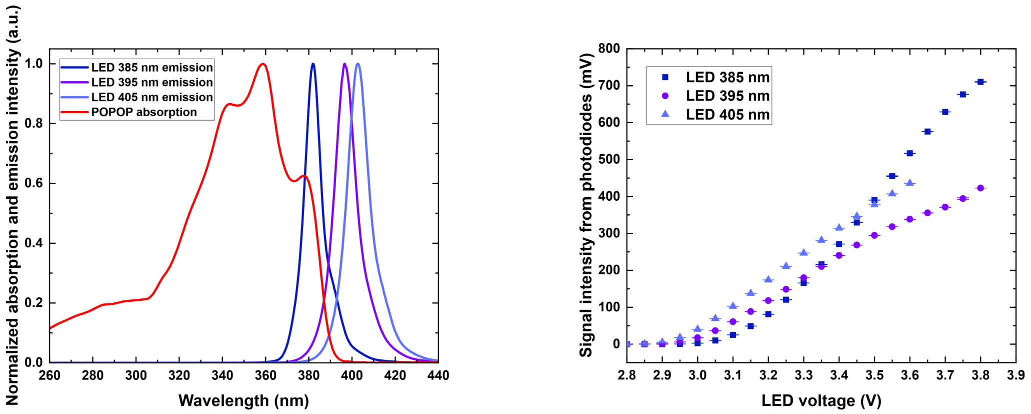

Figure 9. Conceptual description of the plastic scintillator excitation: overlapping of the absorption spectrum of POPOP fluorescent dye in plastic scintillator with the emission spectra of LEDs with different emission characteristics (left), and performance of the setup for light-transfer measurements: voltage signals intensity obtained with the LEDs supplied by a range of voltages (right). The vertical error bars represent one standard deviation from the average voltage measured by the multimeter.

The signal intensity from the photodiodes reading the light from the scintillator, excited by three LEDs as a function of the LED voltage, is presented in the right panel in figure 9. The setup for the light-transfer test has a nonlinear dependency from the LEDs voltage, but in general, the higher the LED voltage, the higher the signal intensity from the photodiodes. The setup works in the entire voltage supply range described in the LEDs data sheets.

For further optical scintillator tests, the LED with a 405 nm emission spectrum was chosen to avoid damaging the scintillator by subjecting it to the higher-intensity UV light that shorter-wavelength LEDs provide. A typical voltage of 3.1 V was supplied to the 405 nm LED, to avoid overheating it, increase its lifetime, and decrease the scattering of the LED light outside the collimator. The average background noise in the setup was equal to 0.026 mV. The background noise was measured with a plastic scintillator inserted to the setup, without LED irradiation; the entire setup was covered to be light-tight. The measured signals from the setup in this configuration are at a level of about 100 mV. The corresponding signal-to-noise ratio is about 3800, which is satisfactory.

The results from light transfer tests are presented in figure 10. The average difference between the 30 mm and 300 mm LED positions read out from the scintillator A side is 5.66 ± 4.04 %. The average difference between the 300 mm and 30 mm LED positions read out from the scintillator B side is 3.85 ± 4.86 %. The average differences and their distributions are below 20%, which indicates that the BC-408 plastic scintillators have good homogeneity. A small number of scintillators have a negative difference value. This means that the signal at the farther LED position was larger than the signal at the closer position, which could be caused by a difference in the 6 mm × 30 mm cross-sections (A and B edges) of the same scintillator strips. Scintillators with a difference larger than two standard deviations from the mean also have high cross-sectional differences at both ends of the same strip. A small fluctuation in the plastic scintillator thickness (6 mm) and width (30 mm) can change the intensity of the light through the cross-section surface (nominally, 6 mm × 30 mm) and finally per photodiode active area. A fluctuation of the plastic scintillator thickness can result in a larger absorption of the exciting LED light by thicker pieces, which thus generate a stronger light signal at their 6 mm × 30 mm cross-section surface.

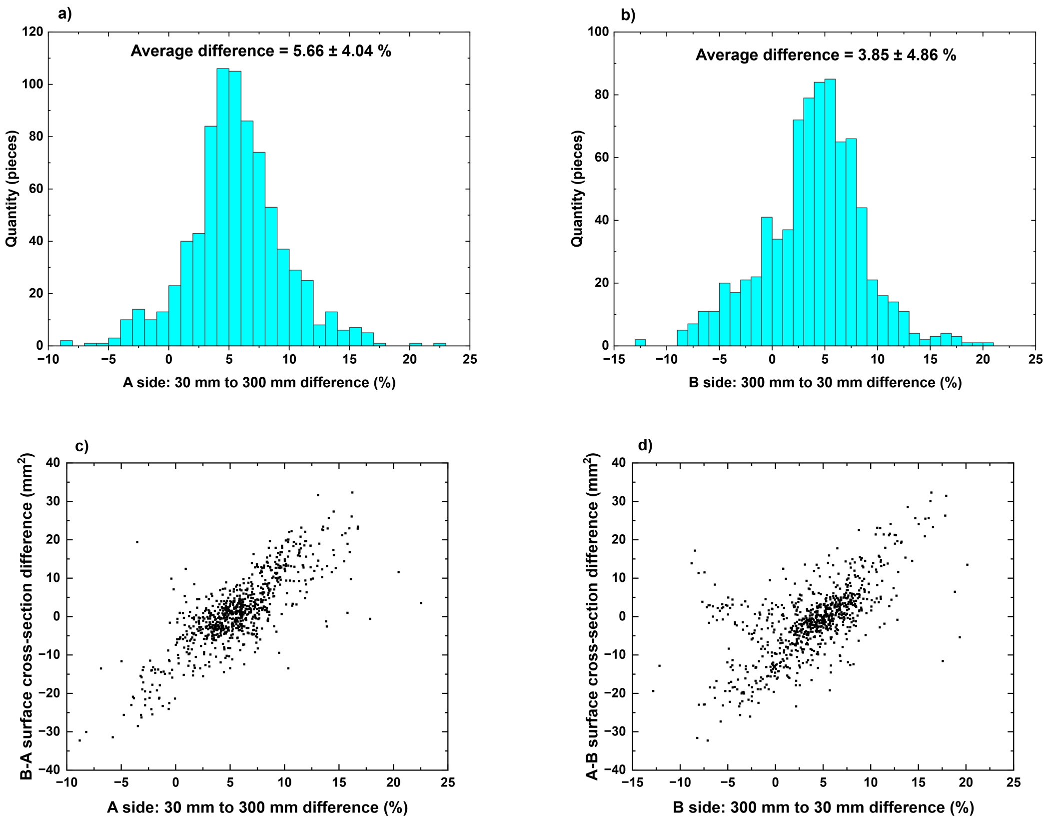

Figure 10. Results of the light-transfer measurements: distributions of percentage signal differences for two positions measured at one photodiode matrix (a, b); the same data plotted versus the surface cross-sections difference between the two ends of the same plastic scintillator strip (c, d).

3.4 Transmittance

The emission and transmission spectra of one BC-408 plastic scintillator sample strip are presented on the left panel in figure 11. The wavelength of maximum emission is equal to 425.8 nm and agrees within the spectrometer resolution with the 425 nm value from the scintillator data sheet. The transmittance at this wavelength point was measured for nineteen scintillators from different batches. The results of the transmittance measurements for different scintillator batches are presented on the right panel in figure 11. The average transmittance of 57 measurements (3 points along each scintillator times 19 scintillators) is equal to 90.54 ± 0.37% and agrees with the transmittance of 90.5 ± 0.2% from our previous measurements [27]. The differences between the transmittance values among scintillator in different batches and the standard deviations measured in each batch are posited to be due to thickness variations in each scintillator, surface defects (such as scratches and pores from the casting process), and variations in the light emitted by the tungsten halogen lamp used in the experimental setup.

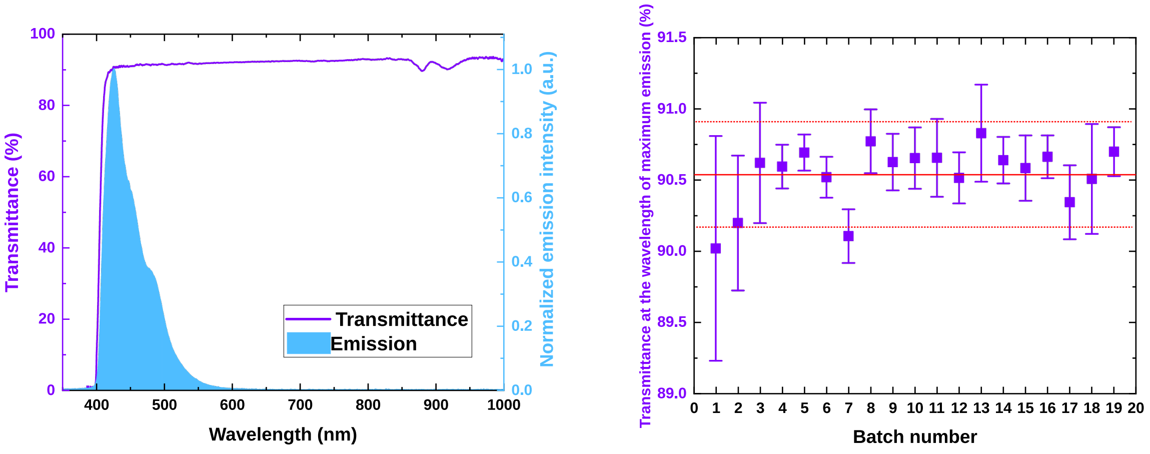

Figure 11. Example of the transmission spectrum of one BC-408 plastic scintillator strip superimposed to its emission spectrum (left), and average transmittance at 425.8 nm of the wavelength of maximum emission point measured for one random selected scintillator from 19 batches of scintillators (right). The error bars represent standard deviation from three transmittance measurements for each 6 mm thick scintillator strip. The horizontal solid and dotted red lines represent the average and one-standard-deviation of the measurements, respectively.

3.5 Technical attenuation length

The emission spectra of one BC-408 plastic scintillator sample strip are presented on the left panel in figure 12. The properties of the emission spectra are presented on the right panel in figure 12. The full width at half maximum (FWHM) of the emission spectrum decreases from 50.33 nm to 41.67 nm as the LED-fiber distance increases from 1 cm to 31 cm. The 50.33 nm value of the FWHM of the BC-408 emission spectrum for a 1 cm LED-fiber distance is very close to the 51.3 nm value of FWHM of the BC-408 emission spectrum measured in our previous work [27]. The emission maximum increases from 427.42 nm to 429.97 nm as the LED-fiber distance increases from 1 cm to 31 cm. The short wavelength part of the spectrum is more attenuated, resulting in a decrease of the FWHM of the spectrum and a shift of its maximum.

The emission intensity at the spectrum maximum (height of the spectrum) decreases exponentially as the LED-fiber distance increases (left panel in figure 13). The TAL short component was measured

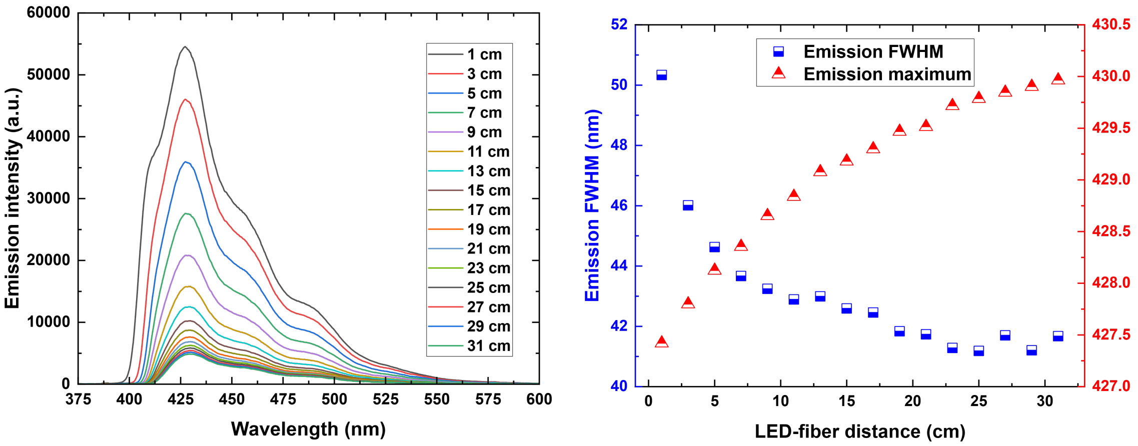

Figure 12. Change of the emission spectra of BC-408 plastic scintillator with respect to the LED-fiber distance (left); properties of the emission spectra: FWHM and emission maximum values (right).

for 19 scintillators from different batches and obtained with the use of the exponential function in eq. (2.2) to fit the emission intensity data points. The results of the TAL short component measurements for different scintillator batches are presented on the right panel in figure 13. The average TAL short component for 19 measured scintillators is equal to 9.49 ± 0.59 cm. The obtained short component values of the TAL of BC-408 plastic scintillators are in the 4–7 cm range, when measured for plastic scintillators with a similar cross-section and of the high-transparency type [26, 27]. The TAL values are scattered around the mean because the TAL measurements of long and thin scintillating optical elements are distributed according to a Moyal distribution [28].

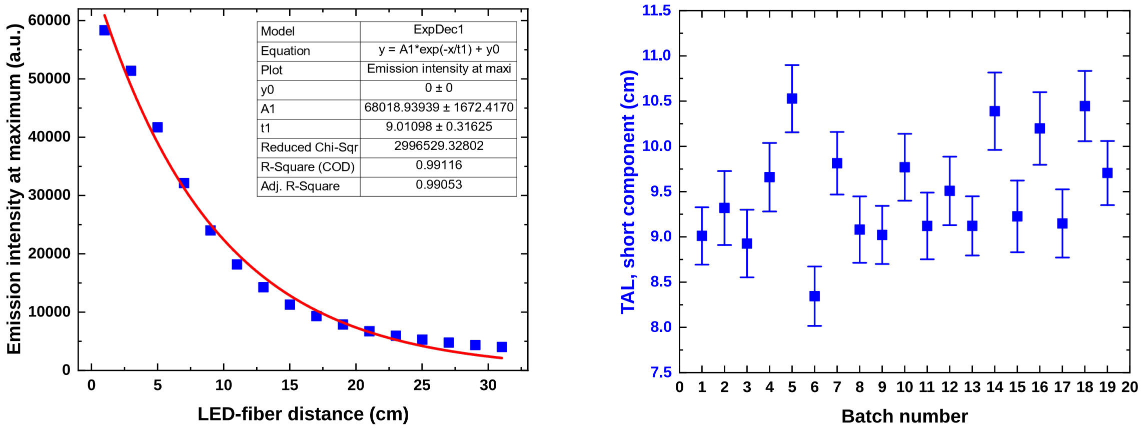

Figure 13. Example of the dependency of the emission intensity at spectrum maximum on the LED-fiber distance for BC-408 plastic scintillators (left); short component of the TAL measured for one random selected scintillator from 19 batches (right). The red line indicates the fit of the data points using the exponential function defined in eq. (2.2). The error bars represent a standard deviation from the fit.

4 Conclusions

The majority of the obtained plastic scintillators meet the transparency criteria and are within dimensional tolerances. The scintillators with a high difference of cross-section dimensions, which affects the light transfer, should be rejected from tomograph construction. The obtained results confirm the high transparency of the ordered BC-408 scintillators for the construction of the long modules of the TB-J-PET scanner. The plastic scintillators have a low attenuation for blue light, emitted at a maximum of 425.8 nm. Small optical signal differences at the level of about 5.66% between both ends of the same scintillator strip will not affect the uniformity of the timing properties along the length of the scintillator in the next generation J-PET scanner.

Acknowledgments

The authors acknowledge the technical and administrative support of A. Heczko, M. Kajetanowicz, W. Migdał and A. Mucha. This work was supported by the National Science Centre of Poland through grants No. 2019/35/B/ST2/03562, 2020/38/E/ST2/00112, 2021/42/A/ST2/00423, 2021/43/B/ST2/02150 and 2023/07/X/ST11/01694, the Ministry of Education and Science through grant no. SPUB/SP/490528/2021, the SciMat and qLIFE Priority Research Areas budget No. U1U/P05/NO/03.27 and "Laboratories of the Young" No. N17/LM/5/KŁ/2022 and LM/13/KŁ/2022-2 as part of the "Excellence Initiative Research University" program at the Jagiellonian University in Kraków.

References

[1] A. Alavi, T.J. Werner, E. Stępień and P. Moskal, *Unparalleled and revolutionary impact of PET imaging on research and day to day practice of medicine*, *Bio-Algor. Med-Syst.* **17** (2021) 203.

[2] S. Vandenberghe, P. Moskal and J.S. Karp, *State of the art in total body PET*, *EJNMMI Phys.* **7** (2020) 35.

[3] R.D. Badawi et al., *First Human Imaging Studies with the EXPLORER Total-Body PET Scanner*, *J. Nucl. Med.* **60** (2019) 299.

[4] J.S. Karp et al., *PennPET Explorer: Design and Preliminary Performance of a Whole-Body Imager*, *J. Nucl. Med.* **61** (2019) 136.

[5] G.A. Prenosil et al., *Performance Characteristics of the Biograph Vision Quadra PET/CT System with a Long Axial Field of View Using the NEMA NU 2-2018 Standard*, *J. Nucl. Med.* **63** (2021) 476.

[6] E. Yoshida, F. Obata and T. Yamaya, *Calibration method of crosshair light sharing PET detector with TOF and DOI capabilities*, *Biomed. Phys. Eng. Express* **9** (2023) 055031.

[7] E. Yoshida, F. Obata and T. Yamaya, *Optical crosstalk of protective cover on MPPC array for TOF PET detector*, *Phys. Med. Biol.* **69** (2024) 125012.

[8] H. Tashima and T. Yamaya, *Compton imaging for medical applications*, *Radiol. Phys. Technol.* **15** (2022) 187.

[9] M. Uenomachi, K. Shimazoe and H. Takahashi, *A double photon coincidence detection method for medical gamma-ray imaging*, *Bio-Algor. Med-Syst.* **18** (2022) 120.

[10] K. Shimazoe and M. Uenomachi, *Multi-molecule imaging and inter-molecular imaging in nuclear medicine*, *Bio-Algor. Med-Syst.* **18** (2022) 127.

[11] P. Moskal and E. Stępień, *Prospects and Clinical Perspectives of Total-Body PET Imaging Using Plastic Scintillators*, *PET Clinics* **15** (2020) 439.

[12] S. Sharma et al., *Efficiency determination of J-PET: first plastic scintillators-based PET scanner*, *EJNMMI Phys.* **10** (2023) 28.

[13] P. Moskal et al., *Simulating NEMA characteristics of the modular total-body J-PET scanner — an economic total-body PET from plastic scintillators*, *Phys. Med. Biol.* **66** (2021) 175015 [`arXiv:2107.01356`].

[14] M. Dadgar et al., *Comparative studies of the sensitivities of sparse and full geometries of Total-Body PET scanners built from crystals and plastic scintillators*, *EJNMMI Phys.* **10** (2023) 62.

[15] F. Tayefi Ardebili, S. Niedźwiecki and P. Moskal, *Evaluation of Modular J-PET sensitivity*, *Bio-Algor. Med-Syst.* **19** (2023) 132.

[16] P. Moskal, B. Jasińska, E. Stępień and S.D. Bass, *Positronium in medicine and biology*, *Nature Rev. Phys.* **1** (2019) 527.

[17] P. Moskal et al., *Positronium imaging with the novel multiphoton PET scanner*, *Sci. Adv.* **7** (2021) eabh4394.

[18] M. Das et al., *Estimating the efficiency and purityfor detecting annihilation and promptphotons for positronium imagingwith J-PET using toy Monte Carlosimulation*, *Bio-Algor. Med-Syst.* **19** (2023) 87.

[19] E.Y. Beyene et al., *Exploration of simultaneous dual-isotope imaging with multiphoton modular J-PET scanner*, *Bio-Algor. Med-Syst.* **19** (2023) 101.

[20] P. Moskal et al., *Testing CPT symmetry in ortho-positronium decays with positronium annihilation tomography*, *Nature Commun.* **12** (2021) 5658 [`arXiv:2112.04235`].

[21] P. Moskal et al., *Discrete symmetries tested at 10^{-4} precision using linear polarization of photons from positronium annihilations*, *Nature Commun.* **15** (2024) 78 [`arXiv:2401.12092`].

[22] P. Moskal et al., *Nonmaximal entanglement of photons from positron-electron annihilation demonstrated using a plastic PET scanner*, *Sci. Adv.* **11** (2025) ads3046 [`arXiv:2407.08574`].

[23] K. Brzeziński et al., *Detection of range shifts in proton beam therapy using the J-PET scanner: a patient simulation study*, *Phys. Med. Biol.* **68** (2023) 145016.

[24] J. Baran et al., *Feasibility of the J-PET to monitor the range of therapeutic proton beams*, *Phys. Med.* **118** (2024) 103301.

[25] K. Parodi, T. Yamaya and P. Moskal, *Experience and new prospects of PET imaging for ion beam therapy monitoring*, *Z. Med. Phys.* **33** (2023) 22.

[26] Ł. Kapłon, *Technical Attenuation Length Measurement of Plastic Scintillator Strips for the Total-Body J-PET Scanner*, *IEEE Trans. Nucl. Sci.* **67** (2020) 2286.

[27] Ł. Kapłon et al., *Comparative studies of plastic scintillator strips with high technical attenuation length for the total-body J-PET scanner*, *Nucl. Instrum. Meth. A* **1051** (2023) 168186 [`arXiv:2407.19465`].

[28] A.E. Baulin et al., *Attenuation length and spectral response of Kuraray SCSF-78MJ scintillating fibres*, *Nucl. Instrum. Meth. A* **715** (2013) 48.

[29] A.B.R. Cavalcante et al., *Refining and testing 12,000 km of scintillating plastic fibre for the LHCb SciFi tracker*, 2018 *JINST* **13** P10025.

[30] V. Senchyshyn et al., *Influence of polystyrene scintillator strip methods of production on their main characteristics*, *Radiat. Meas.* **42** (2007) 911.

[31] P. de Barbaro, *Quality control of the production of the hadron calorimeter for the CDF End Plug Upgrade*, in the proceedings of the *IEEE Nuclear Science Symposium*, Norfolk, VA, U.S.A., October 30–November 5 (1994) [`DOI:10.1109/nssmic.1994.474540`].

[32] V.V. Abramov et al., *Production and quality control of optical elements for the end cap hadron calorimeter of the CMS setup*, *Instrum. Exp. Tech.* **48** (2005) 22.

[33] M. Ellis et al., *The design, construction and performance of the MICE scintillating fibre trackers*, *Nucl. Instrum. Meth. A* **659** (2011) 136 [`arXiv:1005.3491`].

[34] S. Nieswand, *Production and quality assurance of a Scintillating Fibre detector for the LHCb experiment*, 2017 *JINST* **12** C02071.

[35] E. Auffray et al., *Performance of ACCOS, an Automatic Crystal quality Control System for the PWO crystals of the CMS calorimeter*, *Nucl. Instrum. Meth. A* **456** (2001) 325.

[36] Y. Heng, *The two scintillator detectors on BESIII*, in the proceedings of the *IEEE Nuclear Science Symposium and Medical Imaging Conference* (2007), pp. 53–56 `DOI:10.1109/NSSMIC.2007.4436287`.

[37] S. Baccaro et al., *An automatic device for the quality control of large-scale crystal's production*, *Nucl. Instrum. Meth. A* **459** (2001) 278.

[38] B. Borgia et al., *Performance of an automatic bench for scintillating crystal light yield measurement*, *Nucl. Instrum. Meth. A* **426** (1999) 446.

[39] CMS collaboration, *Cross-calibration of two automatic quality control systems for the CMS ECAL crystals*, *Nucl. Instrum. Meth. A* **523** (2004) 355.

[40] K. Ramesh, *Digital Photoelasticity*, Springer Berlin Heidelberg (2000) [`DOI:10.1007/978-3-642-59723-7`].

[41] D. Rinaldi et al., *Quality Control and Characterization of Scintillating Crystals for High Energy Physics and Medical Applications*, in *Wide Spectra of Quality Control*, I. Akyar, ed., InTech (2011) [`DOI:10.5772/24010`].

[42] K. Ramesh and S. Sasikumar, *Digital photoelasticity: Recent developments and diverse applications*, *Opt. Lasers Eng.* **135** (2020) 106186.

[43] M. Lebeau, G. Majni, N. Paone and D. Rinaldi, *Photoelasticity for the investigation of internal stress in BGO scintillating crystals*, *Nucl. Instrum. Meth. A* **397** (1997) 317.

[44] G. Zhao et al., *Characteristics of large-sized Ce:YAG scintillation crystal grown by temperature gradient technique*, *J. Cryst. Growth* **253** (2003) 290.

[45] CRESST collaboration, *Improving the Quality of $CaWO_4$ Target Crystals for CRESST*, *J. Low Temp. Phys.* **209** (2022) 1128.

[46] N. Cocozzella et al., *Quality inspection of anisotropic scintillating lead tungstate (PbWO-4) crystals through measurement of interferometric fringe pattern parameters*, *Nucl. Instrum. Meth. A* **469** (2001) 331.

[47] M. Lebeau et al., *Mapping residual stresses in PbWO(4) crystals using photoelastic analysis*, *Nucl. Instrum. Meth. A* **537** (2005) 154.

[48] D. Rinaldi, A. Ciriaco, M. Lebeau and N. Paone, *Quality control on pre-serial Bridgman production of PbWO(4) scintillating crystals by means of photoelasticity*, *Nucl. Instrum. Meth. A* **615** (2010) 254.

[49] J-PET collaboration, *Time resolution of the plastic scintillator strips with matrix photomultiplier readout for J-PET tomograph*, *Phys. Med. Biol.* **61** (2016) 2025 [`arXiv:1602.02058`].

[50] Ł. Kapłon, *Synthesis and characterization of polystyrene scintillators and their application in positron emission tomography*, Ph.D. thesis, Jagiellonian University, Krakow, Poland (2017).

2025 JINST 20 P09019

[51] Ł. Kapłon et al., *Plastic scintillators for positron emission tomography obtained by the bulk polymerization method*, *Bio-Alg. Med-Syst.* **10** (2014) 27 [`arXiv:1504.06886`].

[52] Ł. Kapłon et al., *Investigation of the light output of 3D-printed plastic scintillators for dosimetry applications*, *Radiat. Meas.* **158** (2022) 106864.

[53] M. Taniguchi and J.S. Lindsey, *Database of Absorption and Fluorescence Spectra of* $>$ 300 *Common Compounds for use in PhotochemCAD*, *Photochem. Photobiol.* **94** (2018) 290.

[54] Ł. Kapłon and G. Moskal, *Blue-emitting polystyrene scintillators for plastic scintillation dosimetry*, *Bio-Algor. Med-Syst.* **17** (2021) 191.